Predictability of Decaying Stratified Turbulence

Martin F. Diaz[a] and Michael L. Waite[b]
Department of Applied Mathematics, University of Waterloo, Waterloo, Ontario, Canada.

Predictability of geophysical fluid dynamics at various scales remains a crucial challenge for accurate weather and climate forecasting. Following the pioneering framework established by Lorenz, numerous studies on homogeneous and isotropic turbulence have demonstrated that flows characterized by diverse scales may exhibit limited predictability. This limitation arises from the inevitable amplification of errors in the initial conditions from small scales to larger scales, even if the initial error is confined to small scales. This research investigates the predictability of freely decaying homogeneous stratified turbulence, which serves as a representative model for small-scale geophysical turbulence where rotational effects are negligible. Direct numerical simulations are employed to assess predictability by analyzing the growth of errors introduced in pairs of simulations with near-identical initial conditions; errors are modeled as the difference field of the pair. Previous studies have established a connection between the finite range of predictability and the slope of the kinetic energy spectrum. In the context of stratified turbulence, the shape of the energy spectrum exhibits a dependence on the buoyancy Reynolds number (Re_b), particularly at lower values of Re_b. This work conducts a comparative analysis of both the energy spectra and the error growth behavior across different regimes of stratified turbulence, encompassing a range of Re_b values from $\mathcal{O}(1)$ to $\mathcal{O}(10)$. The sensitivity of the obtained results to the introduced error is investigated. Modifying the geometrical shape of the error (spherical vs. cylindrical complement) and the cutoff wavenumber while maintaining the initial error kinetic energy did not significantly alter the error dynamics. The results are robust to variations in the method of error introduction.

Keywords: stratified turbulence, predictability, direct numerical simulations, buoyancy Reynolds number

I. INTRODUCTION

Within the realm of geophysical fluid dynamics, the tension between the inherent chaos of turbulence and its finite predictability remains a captivating problem. While turbulence is an inherently chaotic problem, in which minute perturbations rapidly amplify and spread, the degree of predictability in modern numerical simulations, including numerical weather prediction (NWP), is impressive (e.g. Kalnay, 2002).

Following early efforts to tackle the atmospheric predictability problem (e.g. Richardson, 1922; Thompson, 1957), in his pioneering paper, Lorenz (1969) proposed to classify deterministic systems into different categories depending on how they statistically evolve with respect to errors imposed in the initial conditions. Due to sparse observational networks, initial conditions in geophysical fluid simulations inevitably have errors at small scales. Lorenz (1969) studied the evolution of this error with pairs of simulations, the difference of which was called error (and can be considered an example of epistemic uncertainty, e.g. Oberkampf et al., 2002). The main distinction between Lorenz' categories rest on whether at subsequent times the magnitude of the difference between the "real or reference" and the "observed or predictor" system can always be controlled by restricting the initial error to sufficiently small scales or whether it is inevitable that the discrepancy will become large, for any arbitrarily small initial error.

The signature conclusion of Lorenz (1969), when analyzing several experiments, is that errors initially confined exclusively to the smallest scales of motion (i.e. the velocity in

the real and observed systems only differ at a specific range of high wavenumbers, which corresponds to the unobserved small scales) may lead, by a continual process, to errors at the largest scales in a finite time, even as the initial error is restricted to smaller and smaller scales. This is what it is commonly denoted as an *inverse cascade* for the propagation of error and it encapsulates the fact that, in some cases, errors at small scales tend to gradually contaminate the larger scale dynamics. However, the dependency of whether a deterministic system posses an intrinsic range of predictability (i.e. an inherent time interval within which errors surpass any prechosen magnitude) is tightly related with the slope of the inertial range of the kinetic energy spectrum of said system.

Lorenz's groundbreaking work gave birth to the classical school of turbulence predictability, where numerous researchers tried to expand his model or make a distinctive contribution within the subject (Leith, 1971; Lilly, 1972; Leith and Kraichnan, 1972; Herring et al., 1973). The cumulative evidence from these studies lends strong support to the notion that the existence of an inverse cascade of error propagation is a direct consequence of the characteristic shape of the power law in the inertial range of the energy spectrum. Likewise, the amount of predictability described by the rate of error propagation has a direct association with the steepness of the slope of the inertial range. Systems with steeper slopes tend to carry more predictability than those with shallower slopes, which is crucial if we point to the fact that 2D and 3D turbulence differ significantly in that aspect. Let us recall that 2D turbulence usually presents a kinetic energy spectrum with a "-3" power law in the enstrophy cascade (Kraichnan, 1967), whereas 3D turbulence exhibits the famous "-5/3" slope in the energy cascade (Kolmogorov, 1941; Lundgren, 2003). Furthermore, the energy error spectrum $E_\Delta(k,t)$, which is the spectrum of the kinetic energy of the difference of the fields' velocities, grows

---
[a]Electronic mail: mfdiazro@uwaterloo.ca
[b]Electronic mail: mwaite@uwaterloo.ca

with time in a *self-similar* fashion.

Subsequent research reaffirmed and further explored the pioneering findings of the classical predictability school, using closure models, large eddy simulations, and direct numerical simulations (DNS) of different fluid models (Métais and Lesieur, 1986; Chollet and Métais, 1989; Rotunno and Snyder, 2008; Morss et al., 2009; Ngan et al., 2009; Durran and Gingrich, 2014; Boffetta and Musacchio, 2017; Yoshimatsu and Ariki, 2019; Liu et al., 2022; Ge et al., 2023), leading to a richer understanding of predictability across various contexts. For instance, Morss et al. (2009) concluded that in quasi-geostrophic turbulence, the key difference in error behavior between shallow spectral slopes (like -5/3) and steeper ones (like -3) lies in how the kinetic energy spectrum reacts to small-scale errors. In flows with a -5/3 slope, the peak of the error spectrum initially appears at small scales due to their faster turnover time. However, as these scales saturate with errors, the peak shifts towards larger, energy-containing scales, leading to a slowdown in error growth. Conversely, flows with a -3 slope, typical of 2D turbulence, exhibit a constant turnover time across scales. Consequently, the error spectrum peaks at the large scales from the beginning, and saturation of even smaller scales has minimal impact on the overall error growth rate. Concurrently, Ngan et al. (2009) aimed to build a bridge between theoretical understanding of turbulence and the inherent complexities of numerical weather prediction models by studying rotating stratified turbulence. While their primary focus centered on discerning the variations in predictability across various geophysical scales, numerous results can be derived by adopting a similar framework to theirs. In addition, Lorenz's original predictability framework has been expanded and studied within modern NWP models (e.g. Tribbia and Baumhefner, 2004; Lo and Ngan, 2015; Sun and Zhang, 2020).

In their work, Ngan et al. (2009) called for an implementation of modern statistical diagnostics (such as relative entropy or finite-size Lyapunov exponents) from interdisciplinary fields like information theory and complex systems analysis, to act as a much needed complement to the classical picture of turbulence predictability As a response, and building upon some of their prior research (Boffetta and Musacchio, 2001), Boffetta and Musacchio (2017) investigated predictability in isotropic homogeneous stationary turbulence using high-resolution DNS across various Reynolds numbers. They found predictability persists despite turbulence's chaotic nature, attributing it to the ratio between fast perturbation time scales and the time scale for perturbations to significantly influence large-scale dynamics. Their results revealed a Reynolds number dependency on Lyapunov exponents, deviating from dimensional analysis predictions.

Following the above review of predictability, we give a review of the characteristics of stratified turbulence (Riley and Lelong, 2000; Riley and Lindborg, 2008). In the context of atmospheric and oceanic flows, stratified turbulence plays a crucial role because the buoyancy forces (represented by the Brunt–Väisälä frequency N) significantly outweigh the Coriolis force (represented by the Coriolis parameter f). This imbalance, typically observed in mid-latitudes with $N/f \sim 100$,

creates a unique range of length scales where buoyancy dominates. Notably, these length scales roughly correspond to the atmospheric mesoscale (Waite, 2014). It is natural to consider independently the effects on the dynamics of two characteristic length scales inside a stratified fluid: the vertical ($l_\uparrow$) and the horizontal ($l_\leftrightarrow$). Likewise, we need to impose certain restrictions by the means of dimensionless quantities; hence, we require the following conditions to be fulfilled as in Riley and Lindborg (2012):

- The ratio of the inertial forces with respect to buoyancy forces to be small, which implies small Froude number

$$F_\leftrightarrow = \frac{u}{Nl_\leftrightarrow} \ll 1, \tag{1}$$

where u denotes the characteristic velocity.

- Weak rotational effects, which implies a large Rossby number

$$Ro_\leftrightarrow = \frac{u}{fl_\leftrightarrow} \geq 1. \tag{2}$$

On Earth's atmosphere, the range of scales where $Fr_\leftrightarrow \ll 1 \lesssim Ro_\leftrightarrow$ is usually denoted as the *mesoscale* ($\mathcal{O}(100)$ km and smaller), where the effects of stratification are greater than the ones of rotation.

- Large *buoyancy* Reynolds number

$$Re_b = F_\leftrightarrow^2 Re_\leftrightarrow = \frac{u^3}{\nu N^2 l_\leftrightarrow} \gg 1, \tag{3}$$

where we take the Reynolds number as $Re_\leftrightarrow = ul_\leftrightarrow/\nu$ with ν being the kinematic viscosity. As indicated by Brethouwer et al. (2007), for a fixed Re the stratification may suppress turbulence as $F_\leftrightarrow$ decreases, implying that strong stratification requires even larger Reynolds numbers. Re_b is effectively the Reynolds number due to vertical gradients in the horizontal momentum equation when $l_\uparrow \sim u/N$ (Brethouwer et al., 2007).

Typical values in the atmospheric mesoscale are: $U = 10$ ms^{-1}, $l_\leftrightarrow = 100$ km, $N = 10^{-2}$s^{-1}, and $\nu = 10^{-5}$m^{2}s^{-1}, which yields the following dimensionless quantities:

$$Fr_\leftrightarrow = 10^{-2}, \quad Re_\leftrightarrow = 10^{11}, \quad Re_b = 10^7 \tag{4}$$

(e.g. Waite, 2014). However, such large values of Re_b are not attainable in most experiments or DNS, where Re_b is typically $\mathcal{O}(1) - \mathcal{O}(10)$ (e.g. as surveyed by Brethouwer et al., 2007).

Both experimental and numerical set-ups have been essential and complementary to unravel the phenomenology involved with the development of freely decaying and stationary stratified turbulence. On the experimental side, works like Lin and Pao (1979) point to the fact that turbulence initially grows in the usual chaotic manner, thereafter stratification promotes organization of the vorticity structures. Vertical motions are generally inhibited, highlighting the emergence of quasi-two-dimensional structures. For example, Billant and Chomaz (2000) showed how a vertical columnar vortex present a new

kind of *zig-zag instability* due to being immersed in a stratified fluid, noting the formation of horizontal structures as well. These experimental observations coexist in agreement with a lot of their numerical simulation counterparts. For instance, Kimura and Herring (1996) found scattered "pancake-shaped" vortex patches lying in the horizontal plane suggesting them as a good candidate for the final structures in decaying stratified turbulence. The presence of these horizontal layers of eddies is found in multiple references (e.g. Riley and deBruynKops, 2003; Waite and Bartello, 2004; Brethouwer et al., 2007; Maffioli and Davidson, 2016) regardless of the different initial conditions or the introduction of forcing.

The development of isotropic turbulence is famously characterized by the Kolmogorov scale, expressed by

$$\eta = \left(\frac{\nu^3}{\varepsilon}\right)^{\frac{1}{4}}, \tag{5}$$

where ε is the viscous dissipation of kinetic energy per unit of mass. However, due to aforementioned collapse of the vertical scale, it is natural to wonder if there exists a small enough scale such that turbulence would no longer be affected by the effects of stratification. Indeed, if we take the hypothesis from Taylor (1935) for the energy dissipation rate ($\varepsilon \sim u^3/l$) and search for a length scale l_O such that the associated Froude number is unitary (at this scale buoyancy no longer reigns as the main actor in the balance of forces), this yields what it is commonly known as the *Ozmidov* scale

$$l_O = \left(\frac{\varepsilon}{N^3}\right)^{1/2}. \tag{6}$$

According to Riley and Lindborg (2008) this scale can also be interpreted as well as the largest horizontal scale possessing sufficient kinetic energy to overturn. Moreover, we can now rewrite the buoyancy Reynolds number in terms of this characteristic scale as

$$Re_b \sim \left(\frac{l_O}{\eta}\right)^{4/3} \tag{7}$$

(Dillon and Caldwell, 1980; Gargett et al., 1984; Brethouwer et al., 2007).

Lastly, instead of solely analyzing the full kinetic energy spectrum $E(\|\mathbf{k}\|)$, where $\mathbf{k} = (k_x, k_y, k_z)$ is an arbitrary wave vector, it is insightful to separate the contributions from horizontal scales ($k_\leftrightarrow = \sqrt{k_x^2 + k_y^2}$) and vertical scales ($k_\uparrow = |k_z|$). As shown by Lindborg (2006), for the horizontal spectrum, asymptotic analysis reveals ε as the sole shared parameter across scales, leading to a similar form as in isotropic turbulence:

$$E(k_\leftrightarrow) = C_1 \varepsilon^{2/3} k_\leftrightarrow^{-5/3}, \tag{8}$$

which holds whenever $Re_b \gg 1$. For $Re_b \lesssim 1$, the horizontal spectrum gets steeper, reaching magnitudes as steep as k_h^{-5} (Waite, 2014). Similarly, for the vertical spectrum, Riley and Lindborg (2012) highlight that u and N govern the large-scale range, while ε and N dominate the small-scale range. Since N is the only shared parameter, dimensional analysis yields:

$$E(k_\uparrow) = C_2 N^2 k_\uparrow^{-3}. \tag{9}$$

The diverse slopes observed within the stratified turbulence regime present a unique opportunity to explore its behavior within the predictability framework and further analyze its differences from isotropic turbulence. This work utilizes direct numerical simulations (DNS) of stratified turbulence employing a non-hydrostatic Boussinesq model. Various predictability diagnostics are implemented on a baseline case of twin simulations (Section III A). Subsequently, we compare different cases to assess how varying the buoyancy Reynolds number (Section III B) affects predictability, potentially revealing the impact of stratification. Finally, Section III C explores the impacts of varying the error introduction in the twin simulations, evaluating the robustness of our findings.

II. NUMERICAL MODEL AND PROCEDURE

A. Equations of motion

Neglecting the effects of planetary rotation or any other external forces, the Boussinesq equations for a uniformly stratified fluid are:

$$\frac{\partial \mathbf{u}}{\partial t} + \mathbf{u} \cdot \nabla \mathbf{u} = -\frac{1}{\rho_0} \nabla p + b\hat{\mathbf{e}}_z + \nu \nabla^2 \mathbf{u}, \tag{10}$$

$$\frac{\partial b}{\partial t} + \mathbf{u} \cdot \nabla b + N^2 w = \kappa \nabla^2 b, \tag{11}$$

$$\nabla \cdot \mathbf{u} = 0, \tag{12}$$

where $\mathbf{u} = (u, v, w)$ is the velocity field, $\hat{\mathbf{e}}_z$ is the unit vector in the vertical direction, p and ν are the kinematic pressure and viscosity respectively, κ is the thermal diffusivity and we define the buoyancy as $b = -\frac{g}{\rho_0}\rho'$, where the density is decomposed as $\rho = \bar{\rho}(z) + \rho'$, with $|\rho'| \ll \bar{\rho}$ and ρ_0 is a constant reference density. We take the buoyancy frequency

$$N^2 = \frac{g}{\rho_0} \frac{d\bar{\rho}}{dz} \tag{13}$$

to be constant. These equations are useful to portray geophysical fluids across scales, at which stratification is important but Coriolis effects are weak.

We can present equation 10 in terms of the vorticity:

$$\frac{\partial \omega}{\partial t} = \nabla \times (\mathbf{u} \times \omega) + \begin{bmatrix} \partial b/\partial y \\ -\partial b/\partial x \\ 0 \end{bmatrix} + \nu \nabla^2 \omega. \tag{14}$$

Notice that the term in square brackets is the baroclinic generation of vorticity. As a consequence, the vertical component of vorticity is not directly influenced by the buoyancy force.

The main advantage of equation 14 is that if we are able to solve it, via a numerical method, we can always return to our original velocity variable by solving the associated Poisson equation:

$$\nabla^2 \mathbf{u} = -\nabla \times \omega. \tag{15}$$

Elliptic equations such as equation 15 are conveniently solved in their associated Fourier domain. Hence, equation 15 takes the form:

$$-||\mathbf{k}||^2 \hat{\mathbf{u}} = i\mathbf{k} \times \hat{\boldsymbol{\omega}}, \qquad (16)$$

where the hatted variables represent the Fourier counterpart of the original velocity and vorticity. We can readily see that the velocity is obtained by simply dividing the previous expression by the $||\mathbf{k}||^2$ factor. In order to avoid problems at the origin ($\mathbf{k} = 0$), we can consider *all* variables to be zero at the zero wave vector, which can be interpreted as the absence of a uniform mean flow.

B. Numerical model

Our numerical model employs a spectral transform method with periodic boundary conditions on a cubic domain of size L^3, an isotropic grid and with the parameters displayed on table I. We integrate equations 11-14 in time and Fourier space using an appropriate scheme, while storing variables in physical space. The Fast Fourier Transform (FFT) bridges the two domains, allowing us to exploit the most convenient domain for calculations. To mitigate aliasing errors, introduced by point-wise multiplication, we restrict the scales by truncating the number of Fourier coefficients using the "two-thirds rule" at $K_j = n_j/3$ (with $j \in \{x, y, z\}$ and n_j denoting the number of grid points in each direction). This is superior to the *natural* truncation of $K_j = n_j/2$, which is insufficient to counter aliasing errors (Durran, 2010). We use isotropic resolution with $n_j = n$. The equations are solved using a third order Adams Bashford method (AB3), with the viscous and diffusion terms treated with a trapezoidal approach. The timestep dt is chosen for stability to keep the Courant number less than $0.7/\pi$ (Durran, 2010). We are interested in resolving at every point of the grid the whole range of spatial and temporal scales associated with turbulence, from the Kolmogorov scale, up to the integral scale. By this means, our numerical set up is commonly classified as a DNS, which in practice translates to having $\eta K_j \gtrsim 1$ for all $j \in \{x, y, z\}$. We assume unit Prandtl number and set $\kappa = \nu$.

This model is based on established frameworks and has been used successfully to study various problems over the years, including the zigzag instability (Waite and Smolarkiewicz, 2008, appendix A.2), forced stratified turbulence (Legaspi and Waite, 2020) and rotating-stratified turbulence (Waite, 2016).

C. Procedure

Following in the footsteps of several previous numerical studies of predictability (e.g. Lilly, 1972; Leith and Kraichnan, 1972; Métais and Lesieur, 1986; Chollet and Métais, 1989; Morss et al., 2009; Ngan et al., 2009), our general objective is to characterize the *predictability error* that arises from the divergence between almost identical twin experiments that sprout from a common precursor run. Each of the

parent runs presented in this work is initialized with isotropic random-phase velocity fields with a specified energy spectrum following Maffioli and Davidson (2016):

$$E(k) = \mu k^4 \exp(-k^2/k_p^2), \qquad (17)$$

where $E(k) = \frac{1}{2}\langle \hat{\mathbf{u}}^* \cdot \hat{\mathbf{u}} \rangle$ is the three dimensional energy spectrum which is calculated summing over spherical shells of radius k and μ is the amplitude of the initial spectrum. This amplitude is selected to ensure that the initial domain-averaged kinetic energy is normalized to one, meaning that the velocity scale is $\mathcal{O}(1)$. We set $k_p = 5$, which sets the amplitude of the peak of the initial spectrum, located at $\sqrt{2}k_p$. The length scale of our experiments is characterized by this peak as $l = 2\pi/\sqrt{2}k_p \sim 0.89$. We take their initial condition set-up as the base of our simulations because they initialize both potential vorticity and internal gravity waves in stratified turbulence, without giving a particular preference to either of them (Maffioli and Davidson, 2016). From these initial conditions we can estimate the characteristic flow speed using the normalization of kinetic energy and the isotropic set up as follows

$$E = \frac{1}{2}(u^2 + v^2 + w^2) = \frac{3}{2}u^2,$$

therefore $u = \sqrt{2/3}$ and the associated turn over time is $l/u = 1.08$. Notice that we make use of these quantities to calculate the Froude and Reynolds numbers of the initial conditions.

Four viscosities are considered. For each, we let the parent simulation run until nearly reaching full development of turbulence, from 0 to 0.5 time units which is roughly half a turn over time, and gather all the respective model variables. We take those outputs and use them as the initial conditions for the twins simulations, running for an additional 5 time units with the same overall parameters as their parent simulation. Throughout this work we have named the twins *Apollo* and *Artemis*, while identifying the precursor simulation (used as the reference name for each numerical experiment) as different versions of their respective mythological parents (*Jupiter*, *Zeus*, *Leto*, and *Latona*). Keep in mind that the runs are taken sufficiently long –in terms of the characteristic turn over time– that they are able to capture adequately the development and then decay of turbulence. The key point in the twins' set up is that we introduce error to one of them (Artemis), while leaving the other one (Apollo) unperturbed, playing the role of the reference simulation. In this regard, the latter differs initially from the former on account of a small random perturbation introduced at all wavenumbers beyond a defined wavenumber cutoff ($||\mathbf{k}|| > k_c$), which is meant to represent the resolution of the observational network.

Taking this general scheme, we conducted four sets of experiments where we change the value of the viscosity, along with the resolution in accordance with resolving the Kolmorogov scale, while keeping the buoyancy frequency fixed, thus obtaining different values of Re_b. Simulations are referred to by their parent name and resolution n; e.g. Leto (1024) refers to the pair of simulations with $n = 1024$. Consequently, we have changed the amplitude of the introduced error so we have

	Jupiter (256)	Zeus (512)	Leto (1024)	Latona (2048)
ν	2.0×10^{-3}	8.0×10^{-4}	3.1×10^{-4}	1.2×10^{-4}
N	10	10	10	10
Re	363	907	2285	5758
F	0.09	0.09	0.09	0.09
Re_b	2.4	4.6	12.1	35.5
k_O	46	52	51	47
k_d	88	163	331	688
$k_{\max}/k_d$	0.97	1.04	1.03	0.99
dt	0.001	0.0005	0.00025	0.000125

TABLE I. Simulation parameters, non-dimensional numbers, and wavenumbers for all numerical experiments. The number next to the name of the numerical experiment alludes to its resolution n (e.g. Jupiter was set up with a resolution of 256^3). Notice that in order to calculate $k_O = 1/l_O$, $k_d = 1/\eta$ and $Re_b = \varepsilon/(N^2\nu)$ we use the maximum value of dissipation rate (ε) presented on the twin-simulations, while for parameters like Re and F we make use of the initial conditions.

the same initial total error kinetic energy for all the experiments. In this way we can analyse the effects of having different Re and Re_b with same stratification. We use equation 7 to calculate buoyancy Reynolds number.

Afterwards, we explore the effects of error introduction, since it is, by itself, a key factor over all the fore mentioned studies. We emphasize on the implications of the geometry and range of error introduction. Taking our base experiment, Leto (1024), we carried out similar simulations, keeping the same general model parameters and just changing the wavenumber cutoff of error introduction (keeping the same initial total error energy), passing through the Ozmidov wavenumber as it characterizes two separate regions of the stratified turbulence spectrum. Likewise, we conducted an experiment where we added the error in a cylindrical portion of the domain instead of having it introduced by the domain complement of a sphere, making sure that the total amount of initial error keeps the same magnitude as in the base experiment. The advantage of studying so, in the frame of stratified turbulence, is to appraise if a cylindrical geometry would significantly change the results in the horizontal and vertical energy spectrum, as there is an initial contribution of error at every horizontal plane.

D. Diagnostics

In order to assess and quantify the amount of error propagation, we used a compilation of diagnostics presented across the numerical predictability literature (such as Leith and Kraichnan (1972); Chollet and Métais (1989); Ngan et al. (2009)). An immediate first tool, having the velocity fields of each twin, is to calculate the (3D, horizontal and vertical) ensemble energy spectrum at each timestep. Although this does not tell us much about predictability, we can compute in a similar manner the error energy spectrum, which measures the wavenumber distribution of the decorrelation between the two fields. Given our periodic boundary conditions, we can define this quantity as the kinetic energy spectrum of the *dif-*

ference of the velocity fields as follows

$$E_\Delta(k,t)\delta = \frac{1}{2}\sum_{\mathbf{k}'\in\mathscr{I}} ||\underbrace{\hat{\mathbf{u}}_p(\mathbf{k},t)}_{Apollo} - \underbrace{\hat{\mathbf{u}}_r(\mathbf{k},t)}_{Artemis}||^2, \quad (18)$$

where

$$\mathscr{I} = \{\mathbf{k}' | k - \frac{\delta}{2} \leq k' < k + \frac{\delta}{2}\},$$

$\delta = 2\pi/L$, $\hat{\mathbf{u}}$ corresponds to the velocity in the Fourier domain and the subscripts p and r denote Apollo and Artemis, and similarly for $E(k_\leftrightarrow)$ and $E(k_\uparrow)$. The next step is to quantify the ratio of the ensemble and error spectra. Thus, the ratio energy spectrum is defined by

$$R(k,t) = \frac{E_\Delta(k,t)}{E(k,t)}. \quad (19)$$

It is important to recall that Leith and Kraichnan (1972) showed that in both isotropic 2D and 3D turbulence this ratio spectrum develops and moves towards lower wavenumbers in a "self-similar" form (*i.e.* it retains its shape and scaling properties as it evolves in time). Notice that for an arbitrary wave vector $\mathbf{k}_0$, we can express the error kinetic energy as

$$2\cdot\underbrace{\frac{1}{2}\left(\frac{\|\hat{\mathbf{u}}_p(\mathbf{k}_0,t)\|^2}{2} + \frac{\|\hat{\mathbf{u}}_r(\mathbf{k}_0,t)\|^2}{2}\right)}_{\text{Ensemble KE}} - \underbrace{\text{Re}\{\hat{\mathbf{u}}_p(\mathbf{k}_0,t)\cdot\hat{\mathbf{u}}_r^*(\mathbf{k}_0,t)\}}_{\text{Correlation}}, \quad (20)$$

where the ensemble KE refers to the average of the kinetic energy of each of the twins. Therefore as the fields reach full decorrelation at a given scale, the preceding function reaches its maximum value at $R(k,t) = 2$, in which case we will consider that the error is saturated.

As it is rather challenging to interpret all the implications and subtleties by looking just at spectra, it is convenient to consider time series that illustrate the overall error evolution. For instance, the total error kinetic energy is

$$e(t) = \sum_k E_\Delta(k,t), \quad (21)$$

which describes the total amount of dissimilitude between velocity fields and summarizes the *global* error propagation. The error kinetic energy at the time of error introduction is $e(0.5) = 3.97 \times 10^{-5}$, which is 0.004% of the initial ($t = 0$) kinetic energy. Nonetheless, our main interest lies in the *local* (in scale) error dynamics since the existence of an inverse error cascade is usually attributed to the interaction between neighboring scales. For that reason, we have incorporated the time series of the error ratio at given scales of interest, namely: $r_K(t) = R(K,t)$.

The last implemented diagnostic is also heavily inspired by the error inverse cascade. Under the premise of a progressive phenomenon, given the insertion of error at small scales, we are interested in characterizing the wavenumber from which the error has contaminated all the subsequent scales at any given time. This is commonly referred as the error wavenumber or error wavefront (Chollet and Métais, 1989; Ngan et al.,

2009) and is defined by the wavenumber at which the ratio spectra reaches a pre-established threshold:

$$\kappa_e(t) : R(\kappa_e, t) = \gamma, \tag{22}$$

with $\gamma \in (0, 2)$. One immediate advantage is that κ_e describes the time evolution of error locally.

Even though several studies take $\gamma = \frac{1}{2}$ (inspired by Lorenz's original interest in the doubling error time), Chollet and Métais (1989) argue that this quantity should be small enough in order to place the wavenumber κ_e both in the correct range of error spectrum (k^4 for isotropic decaying turbulence) and in the rage of explicitly computed wave numbers. Following Chollet and Métais (1989), we have taken $\gamma = 0.01$. Note that $\kappa_e(t)$ is expected to be a monotonically decreasing function as the front propagates to larger scales and previous studies have obtained a respective power-law scaling for this quantity (Leith and Kraichnan, 1972; Chollet and Métais, 1989).

III. RESULTS

A. Leto (1024), in depth

In order to understand the overall evolution of the experiments and the contrast between them, we first show a detailed dissection of a single experiment: Leto (1024). In that way, the reader becomes better familiarized with stratified turbulence simulations and the interpretation of the subsequent results.

We first exhibit the vorticity fields in figure 1. We compare the time progression of the y-component of vorticity in the Π_{XY} and Π_{YZ} planes. In the first row, at $t = 0.5$, we can observe the general initial evolution of all our numerical experiments. The isotropic random-phase velocity fields have just barely developed and, as a result, we encounter a similar picture across the different planes. In other words, at the time of the conception of the twins, the turbulence has not significantly lost its isotropic nature inherited from the initial conditions. At the subsequent times ($t = 2.9$ and $t = 5.30$), the full display of anisotropy is observed, as the vertical slices show how the turbulence unfolds and organizes in horizontal layers. On the right panel, layers of strong shear are clearly visible, especially at later times, along with disturbances resembling shear instabilities (as observed in e.g. Riley and deBruynKops, 2003; Brethouwer et al., 2007). Lastly, on the third row, we can identify that the stratification has organized those instabilities in wider horizontal layers on the right panel, which is a direct reference to the famous pancake-eddies addressed earlier. As time goes by, the overall vorticity magnitudes decrease as expected when dealing with decaying turbulence.

Next, we discuss the time series of two important quantities that characterize turbulence. In the top panel of figure 2 we have the kinetic energy dissipation rate of both twins. As expected, the time series are identical for $t \in [0, 0.5]$ (as this part represent the parent run), but once the error is introduced we can see a significant jump for the perturbed twin

Artemis. This shouldn't be surprising, as we have abruptly changed the small scales by introducing the error kinetic energy, some of which is rapidly dissipated, leading to a short increase in dissipation in the perturbed twin. After that jump, we can see that both graphs share a similar path, as expected from Taylor's hypothesis (Taylor, 1935) that the dissipation is determined by the large scales. In other words, the dissipation rate of Artemis returns to the expected value as determined by the unperturbed large scales. If we take a look at the bottom panel of figure 2, we can appreciate the hierarchy of the large scales as well. There we can see that in spite of altering the domain averaged energy while adding the perturbations, as they are introduced at small scales, they do not cause a significant change as the mean energy is dominated by the large scales.

Now, to transition towards the predictability diagnostics, we commence by introducing the ensemble kinetic energy spectra in terms of total, horizontal and vertical wavenumbers at different times (figure 3). If we concentrate our attention on the first couple of outputs at times $t = 0.5$ and $t = 1$, we can observe that the initial spectrum is steep and then, as the dissipation increases, the spectrum gets shallower, which is characteristic of decaying turbulence. We can also see that the spectra are equally spaced at the beginning and then they start to get closer, for large wavenumbers. As these figures are set in a logarithmic scale, given the spacing between lines, we may infer an exponential decay at early times. Moving on to the horizontal and vertical counterparts of the ensemble spectra, there is a clear distinction with respect to the general shape and slopes. For instance, the horizontal spectra resembles in both aspects the 3D spectra, having that concentration of spectra at large scale (there is less decay at the smallest wavenumbers and more distance between spectra as $k_\leftrightarrow$ gets larger) and a somewhat similar slope. On the other hand the distinctive shape of the vertical spectra helps us to understand the anisotropy of this type of turbulence as well. Here the spacing between lines is similar across all vertical wavenumbers at early times.

As discussed in section II, we can begin exploring the real consequences of the addition of perturbations regarding predictability by referring to the error spectra. Spectra of error KE are shown in figure 4. We can observe how the initial error is introduced by looking at the lightest spectrum of the top panel in figure 4. Keeping in mind that the error is introduced at $k \geq 20$, then the initial 3D spectrum has naturally the shape of a step function. Moreover, the error grows hastily over all possible wavenumbers in a rather explosive fashion. Right away, the error grows very high at large k, but it is relatively low for small wavenumbers. We can also see that the spectrum develops in a "self-similar" fashion, which alludes to the fact that it retains the same shape as the error propagates towards larger scales. As elaborated upon by Ngan et al. (2009), the self-similar nature of the turbulence cascade of energy most likely yields the self-similar behavior of the error spectra.

Following the time evolution of the spectra, we can appreciate the emergence of two distinctive regions due to their contrasting behavior, as highlighted by the arrows in the top panel of figure 4. At large scales the error grows progressively
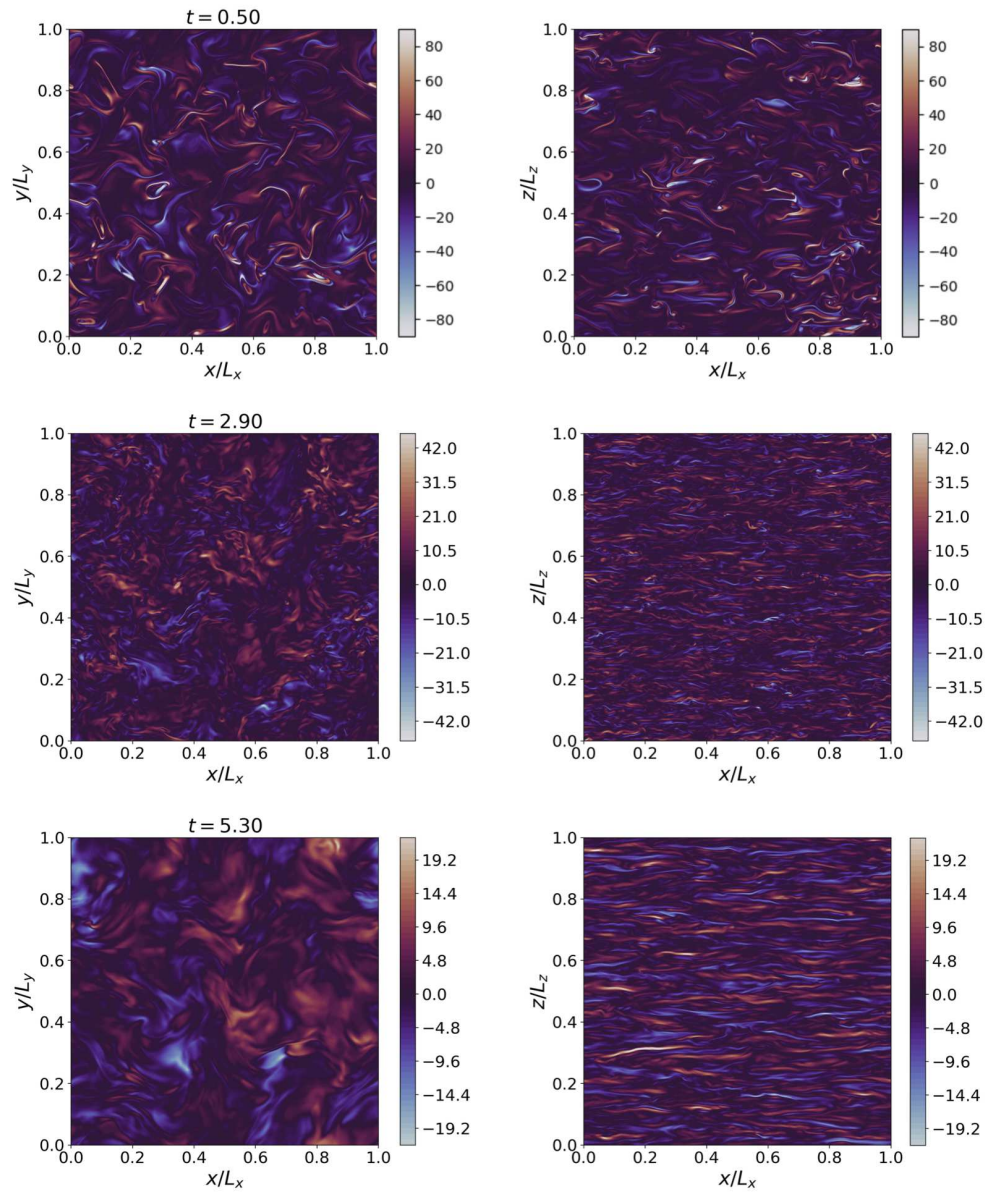
FIG. 1. Slices of the *y*-component of vorticity taken at the middle of the domain of Leto (1024). From left to right column, the Π_{XY}, Π_{XZ} planes are respectively displayed, marking their temporal development with each row (from top to bottom: t = 0.5, 2.9, 5.3).
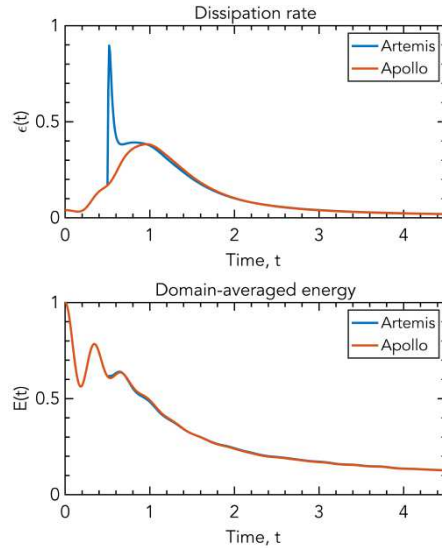
FIG. 2. Time series of domain averaged kinetic energy dissipation rate and kinetic energy of each twin simulation for Leto (1024).
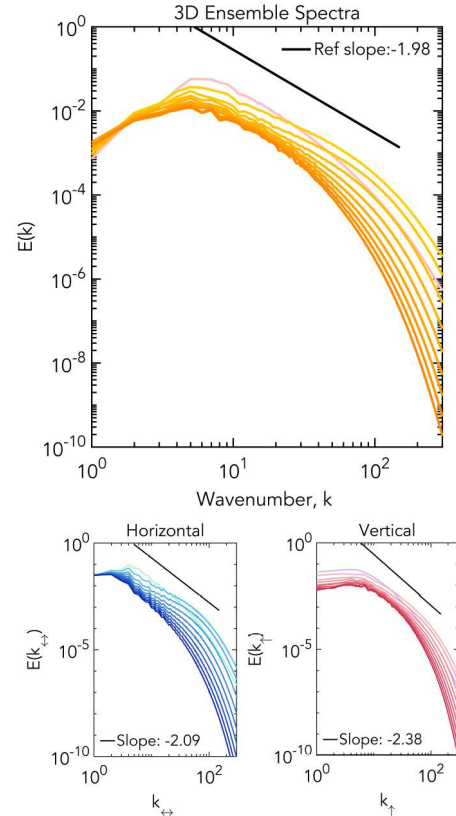

FIG. 3. On top, we have the 3D ensemble kinetic energy spectra of Leto (1024); on bottom, the horizontal and vertical ensemble spectra of Leto (1024) are presented. The time progression is given by the color gradient at each spectral line, from lighter to darker tones. The spectra are plotted each 0.5 time units from 0.5 to 5.5, highlighting the spectrum at t=0.5 with a different color. The reference slope is calculated at the time of maximum dissipation for the unperturbed twin, which roughly coincides with one turnover time.

–characterizing the famous inverse error cascade–, while at small scales, the error saturates quickly and then decreases mainly because of the decaying nature of our experiment. Even though it is difficult to assign a clear separation between those regions, notice that there is an intermediate range of scales, around $k \sim 10$, where both error growth from the inverse error cascade, and turbulent decay, are present. This intermediate scale may be a function of the buoyancy Reynolds number and its meaning could become relevant for further research.

An interesting story unfolds when we decompose the error spectra into horizontal and vertical wavenumber components as shown in the bottom panels of figure 4. Starting with the shape of the initial error spectrum, we have a line with positive slope for the horizontal wavenumbers, while it is a constant for all the vertical wavenumbers. This is a direct consequence of the geometry involved with the error introduction. Remember that we have introduced random noise with a constant amplitude for all wave vectors such that $k \geq 20$ (*i.e.* filling the cube in Fourier space with error outside the sphere of radius 20). In that way, if we sweep through vertical wavenumbers, we would find the same amount of error in each plane with exception of those planes that pass through the empty sphere; however, the cross-section of the sphere space is negligible with respect to the total amount of wavenumbers, the result is an almost constant distribution for the initial error spectrum. Analogously, as we go to larger $k_{\leftrightarrow}$ (now with cylinders) the amount of error grows proportionally to the radius, having as

a result a linear initial horizontal spectrum. After the initial error introduction, we have two completely different stories. For the horizontal spectra, there is a similar inverse cascade of error using the same arguments as in the isotropic case. Whereas for the vertical spectra, the error grows uniformly and instantaneously to *all* possible vertical scales from $t = 0.5$ to 1.0, after which it decreases. There is no visible inverse cascade of error in vertical scale.

Lastly, we have the error ratio spectra presented in figure 5. These figures complement the picture of predictability on stratified turbulence due to their discernible characteristics.
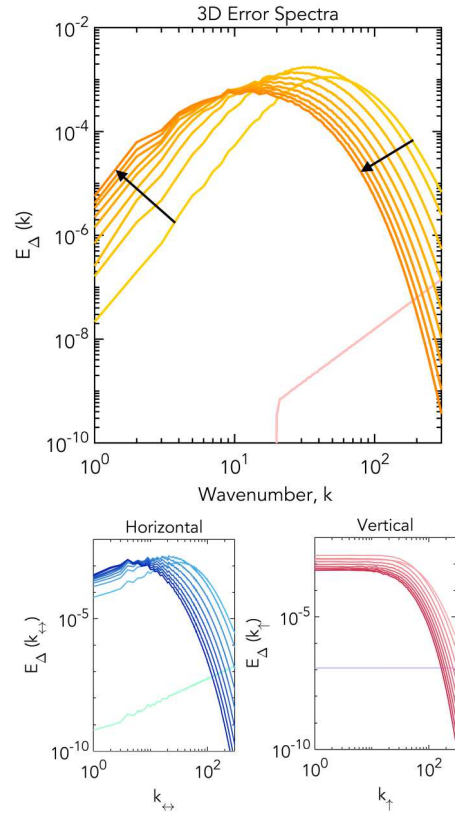
FIG. 4. The top panel displays the 3D error kinetic energy spectra of Leto (1024). The arrows are added to emphasize the time evolution direction of the spectra. Below, the horizontal and vertical error spectra for Leto (1024) are presented. All the spectra are plotted each 0.5 time units from 0.5 to 5.5, highlighting the spectrum at t=0.5 with a different color.
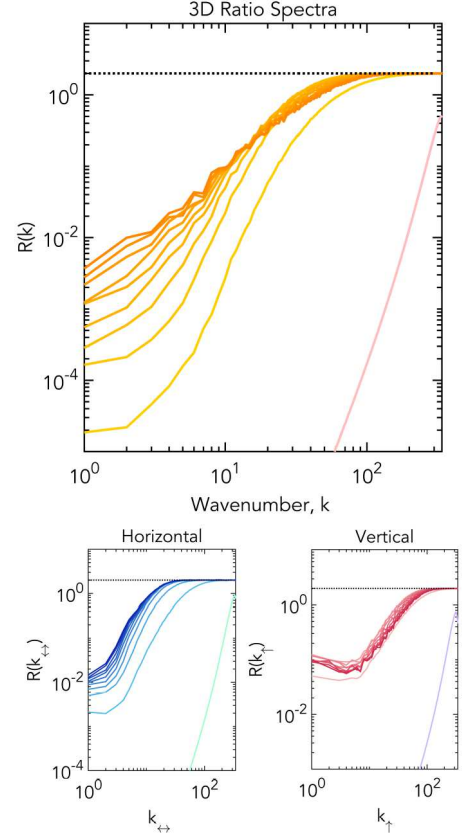
FIG. 5. 3D error ratio spectra of Leto (1024) on top and horizontal and vertical error ratio spectra on bottom. The dotted reference line is a constant at $R(k) = 2$, which denotes the saturation value of the error ratio. The spectra are plotted each 0.5 time units from 0.5 to 5.5, highlighting the spectrum at t=0.5 with a different color.

Starting with the 3D wavenumber, the error propagation towards larger scales is evident, as the spectra move to smaller wavenumbers. In fact, we can appreciate that the error saturates rather quickly for $k \gtrsim 70$, which means that for small scales there is an almost instantaneous complete loss of predictability as both twin fields present total decorrelation between each other. At an intermediate scale, we can see how far upscale the loss of predictability extends by focusing on an arbitrary threshold. For instance, $R(k) \geq 1$ for all $k \geq 30$ at $t = 1$, right after the initial spectrum, before gradually decreasing. In fact, at the end of the run, $R(30) \sim 0.5$. If we were dealing with forced turbulence instead, it is likely that the error would have had the opportunity to contaminate and

saturate even larger scales.

The horizontal and vertical decomposition of error ratio spectra neatly corroborates the assertion of an inverse error cascade for the horizontal case, and the lack of it for the vertical case. That is due to the fact that in the left panel of figure 5, we can notice the same type of self-similar and continuous growth of error towards smaller horizontal wavenumbers, while in the right panel the relative error grows just in the first couple of outputs, then it stabilizes and remains practically the same for the subsequent times. For the vertical spectra, the error dynamics are mostly driven by the decaying nature of turbulence instead. Even though the error dynamics are different, we still observe error saturation for the small scales in

both horizontal and vertical spectra. Indeed, for the horizontal ratio spectra the range of saturated wavenumbers is even wider than in the three-dimensional case, beyond $k_{\leftrightarrow} \sim 30$ there is full saturation of error; whereas in the vertical ratio spectra, the saturation interval starts around $k_{\uparrow} \sim 80$. These results are consistent with our stratified turbulence cartoon of pancake eddies. The independence or decorrelation between layers translates to a rapid loss of predictability at all vertical scales, deviating from the cascading behavior observed in horizontal flows. Horizontal error growth is subject to the horizontal vortical structures and eddies, leading their error dynamics to resemble the classical isotropic inverse cascade scenario, where energy flows towards larger scales. We can argue that the overall amount of predictability in the three-dimensional case is therefore a result of the different predictability contributions from the vertical and horizontal wavenumbers, and the balance between them.

B. Predictability dependency on buoyancy Reynolds number

Now that we are familiarized with the schematic methodology and analysis, we exhibit four experiments with the same stratification, keeping the buoyancy frequency fixed at $N = 10$, while decreasing the viscosity (and therefore increasing the resolution) in order to gradually increase Re and Re_b as displayed in table I. Notice that as Fr is being held constant for all the experiments, we cannot effectively distinguish the dependence of the results with respect to Re or Re_b. However, we have decided to keep the focus on the buoyancy Reynolds number as it is a critical parameter that distinguishes between different flow regimes in stratified turbulence (Brethouwer et al., 2007).

Regarding the predictability insight that these experiments can offer us, we would beforehand expect all of them to exhibit an inevitable loss of predictability. That is because they would fall into the *third* predictability category of Lorenz (1969), which states that the error of flows with spectrum slope shallower than -3 cannot be reduced no matter how small the initial error is taken. At first sight, this premise could be further extended to the horizontal and vertical ensemble spectra. However, there is a clear distinction between the behavior of these last two. Keep in mind that numerous studies indicate the existence of a direct energy cascade for the horizontal spectrum (Lindborg, 2006; Brethouwer et al., 2007), whereas it is not the same case for the vertical scales. Therefore, even though the vertical spectra present a shallow slope (compared to -3), this does not automatically implies the existence of an inverse cascade of error as set out in Lorenz's framework.

The error ratio spectra are presented in figure 6. This diagnostic allows us to quantify the growth of the relative error normalized by the amount of ensemble kinetic energy. For this quantity, the effects of the buoyancy Reynolds number are most contrasting, as we don't see the exact same story unveiling through the panels. At first glance, the Jupiter (256) behavior is notably different. That is because the error at large wavenumbers has not been able to saturate as in the

case of Leto (1024) or even more evidently in the case of Latona (2048), due to the strong viscous effects in Jupiter (256), which has $Re_b = 2.4$. This aspect is difficult to discern by looking at the ensemble spectra and error spectra on their own; however, with the ratio spectra we are able to observe the speed at which a wide range of small scales end up decorrelated and the progression of error contaminating neighbouring scales. Even though the relative amount of saturated scales with respect to the total range of wavenumbers grows as Re_b increases, we can recognize that the region dominated mainly by decaying error –which was unable to reach full saturation– is in $10 \lesssim k \lesssim 100$ for all the experiments. Likewise, we can appreciate how the relative error of the largest scales (take $k = 1$ for example) gets gradually bigger. This breakdown allow us to state that the stratified flows are less predictable as the buoyancy Reynolds number increases. However, this assertion is limited given that this study does not assess the separate dependence on Re_b and Re, since our simulations have fixed Fr.
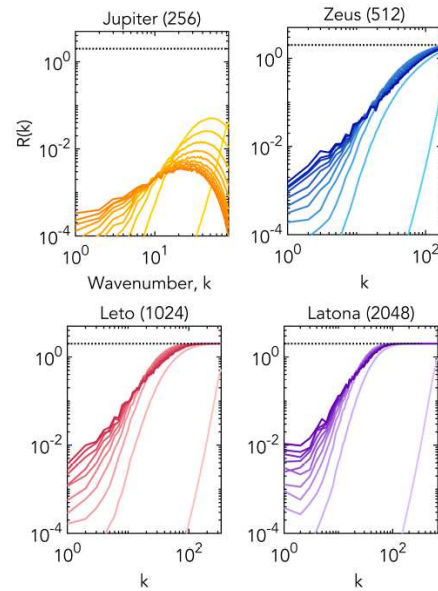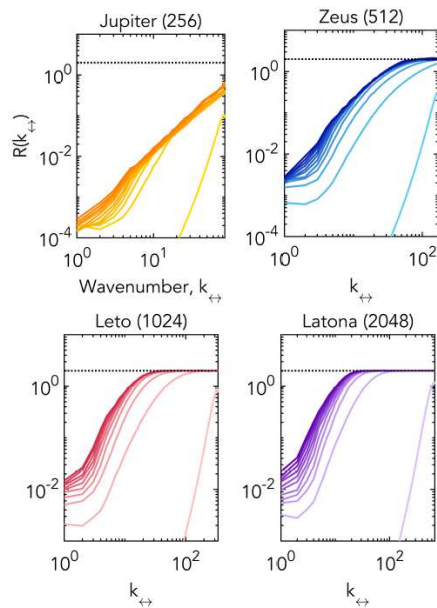

FIG. 6. Error ratio spectra of Jupiter (256), Zeus (512), Leto (1024) and Latona (2048). The spectra are plotted each 0.5 time units from 0.5 to 5.5.

Proceeding with the horizontal ratio spectra in figure 7, the predictability trend of the isotropic case is well preserved as expected. Starting with Jupiter (256), which does not exhibit error saturation at any horizontal scale, there is still a backward propagation of error at small horizontal wavenumber. It seems that the relative error tends to a rather linear distribution (in log-log scale) instead of a self-similar curve as in the

other experiments with higher Re_b. Moving on to the rest of the experiments, we still can see that there is a wider range of saturated scales in comparison to the 3D wavenumber case. In fact, unlike the three dimensional case of error ratio spectra, in figure 7 the horizontal energy ratio spectra of all the experiments trace a continuous evolution towards larger scales –as smaller scales become completely decorrelated– without any visible *decaying* region. Besides that, all the experiments share qualitatively the same behavior. The observation that the horizontal error cascade behaves more similarly to 3D isotropic turbulence than the 3D wavenumber case aligns with the proposed existence of a horizontal energy cascade reported in various studies of stratified turbulence (e.g. Lindborg, 2006; Brethouwer et al., 2007).

FIG. 7. Horizontal error ratio spectra of Jupiter (256), Zeus (512), Leto (1024) and Latona (2048). The spectra are plotted each 0.5 time units from 0.5 to 5.5.

In figure 8 we present the vertical error ratio spectra. Here, as Re_b increases, the final spectrum seems to stay constant at large scales, with a linear distribution for intermediate scales and it ends with the saturation region. Even though the dissipative nature of turbulence plays a leading role on predictability (or the loss of it to be more precise), we can observe that it presents a stronger influence on the vertical scales than in the horizontal ones. Notice that the saturation region is practically entirely defined in the second spectral line, which corresponds to $t = 1$, or around half a turnover time after the birth of the twins.
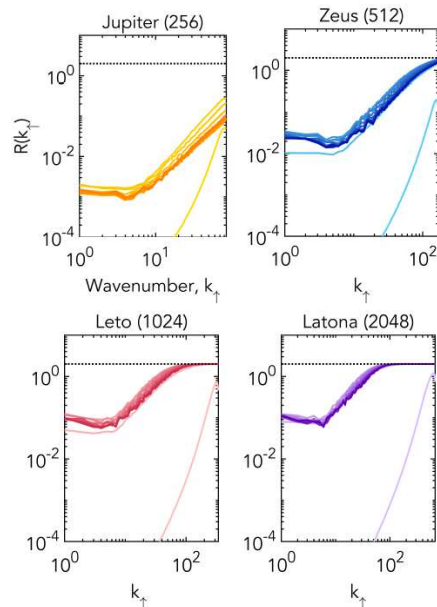

FIG. 8. Vertical error ratio spectra of Jupiter (256), Zeus (512), Leto (1024) and Latona (2048). The spectra are plotted each 0.5 time units from 0.5 to 5.5.

Moreover, it is interesting to examine the range of wavenumbers at which the error is saturated to assess its possible connection to Re_b for both horizontal and vertical wavenumbers. We can characterize the saturation range by identifying the smallest wavenumber at which the horizontal error ratio spectra approaches an arbitrary value near saturation. To illustrate, consider the smallest wavenumber at which $R(k_\leftrightarrow) > 1.8$ across the panels of figure 7, which represents an almost fully saturated scale. Keeping in mind that Jupiter (256) does not reach values ever so close to saturation, we can move on and see that Zeus (512) reaches this value at $k_\leftrightarrow = 55$, Leto (1024) at $k_\leftrightarrow = 25$, and Latona (2048) at $k_\leftrightarrow = 20$. Likewise, in Figure 8, we can see that Zeus (512) reaches this value near saturation at $k_\uparrow = 160$, Leto (1024) at $k_\uparrow = 70$, and Latona (2048) at $k_\uparrow = 60$. Hence, for both horizontal and vertical wavenumbers, the error saturation range extends to smaller wavenumbers as Re_b increases. We notice that even though Re_b increases in a similar proportion from Zeus to Leto and from Leto to Latona, the saturation range does not extend by the same proportion, pointing to possible convergence of the saturation range for increasing Re_b or infer to a non-linear relationship between the saturation range and Re_b.

All of these results are a direct consequence of the characteristic anisotropy presented in stratified flows. Let's resume

our discussion from section III A, regarding the extent of the saturation regions with respect to k, $k_\leftrightarrow$ and $k_\uparrow$. In the case of Latona (2048), structures with $k_\leftrightarrow \sim 20$ –where the error starts to saturate– must be associated, because of anisotropy, to larger $k_\uparrow \sim 60$ in order to reconcile the outcome of the isotropic wavenumber.
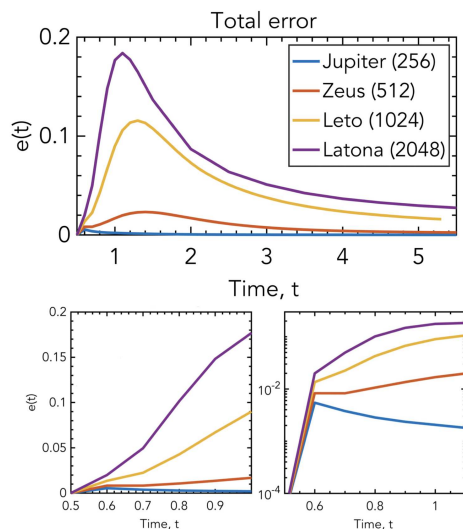

FIG. 9. At the top panel, the total kinetic energy error time series for Jupiter (256), Zeus (512), Leto (1024) and Latona (2048) is presented. In the bottom-left panel, we present a closer look at the same total error from $t = 0.5$ to $t = 1$ with linear axes scales. In the bottom-right panel, we present the same time series but with log-y-axis.

Lastly, we present the time series analysis, starting with the top panel of figure 9, which displays the total error kinetic energy for each of the four experiments of this section as a function of time. In that panel, we can observe how the spatial average of the difference energy between fields increases at first and reaches a global maximum. That is a straight consequence of the propagation and saturation of error in general. Notice that the global maxima gets higher and is reached at earlier times as the buoyancy Reynolds number increases. The amplitude increment may be attributed to the wider range of small scales (which saturate faster) existing in the higher resolution experiments; nevertheless, we have to acknowledge that this diagnostic only contains global information, so there is likely a shared contribution across scales. Subsequently, the function decreases as turbulence decays. In the bottom panels of figure 9, we take a closer look at the initial development of the total error. This particular emphasis has been previously taken in some other studies, (e.g. Boffetta and Musacchio, 2017; Ge et al., 2023), where the initial growth rate was found to be exponential. Even though we observe a rapid growth of the error energy at early times in our experiments,

the bottom-right panel of figure 9 fails to rigorously determinate due to the limited time resolution of the error energy field.

One important thing to remember looking back at the spectral analysis is that we have a wider range of wavenumbers as simulations grow in resolution (as a result of decreasing the viscosity to increase the Reynolds number), which can represent an inconvenience when trying to directly compare them by eye. For that reason we show in figure 10 the time series of the relative error $r_K(t)$ at three different scales shared by all experiments which gives us a more detailed picture of what is happening at a local scale. For instance, at the smallest wavenumber $k = 1$, $r_1(t)$ *just* exhibits a steady growth, as the cumulative result of the backwards error propagation to the largest scales; in addition, we can see that the error ratio at $k = 1$ increases with increasing Re_b. At $k = 10$, after the initial surge of relative error, we see that the growth of the error ratio stagnates across all the experiments, resulting in a concave function. Going back to figure 6, it is around this scale where we were able to identify the fore mentioned *balance* scale. The similar shape, but different amplitude between the cases is remarkable, as they present consistent local error dynamics apparently modulated by the amount of total error.

At $k = 60$ the error ratio immediately reaches values close to saturation followed by a subtle decrease after approximately one turn-over time. It is important to notice that there is a considerable jump in the behavior of the functions as we go from Zeus (512) to Leto (1024) across the last two panels. On the other hand, it is remarkable how close the Leto (1024) and Latona (2048) ratios are to one another for $k = 10$ and $k = 60$, even though there is a significant difference in their buoyancy Reynolds numbers and in their total error energy.

At the end of this section, we turn our attention to the crossover wavenumber or error wavefront presented in figure 11, that is the scale at which the error ratio reaches a certain threshold as it propagates towards larger scales. Given that Jupiter (256) is not able to exhibit the full development of an inverse cascade, we only display the diagnostic on Zeus (512), Leto (1024) and Latona (2048).

Both the isotropic and horizontal wavefronts present a negative power law progression with $\kappa_e(t) \sim t^{-1}$, in close agreement with previous studies such as Leith and Kraichnan (1972) and Chollet and Métais (1989). The slope of the power law for the hortizontal wavenumber wave front (−1.34) is steeper than that for the isotropic wavenumber, and it aligns even closer to the $\kappa_e \sim t^{-3/2}$ scaling derived by dimensional analysis and later corroborated by the numerical findings in 3D isotropic turbulence, as highlighted by Boffetta and Musacchio (2017). This lends more support to the preceding claim that horizontal scales exhibit a stronger resemblance to those observed in 3D turbulence.

There is no similar behavior for the vertical wavenumbers as the error propagation perish rapidly, which we would expect as there is no inverse cascade of error in vertical wavenumber. Despite having a similar behavior, we can observe how there is a stronger backwards propagation of error for $k_\leftrightarrow$ inasmuch as having a steeper slope in comparison with the isotropic wavefront. In fact, the horizontal wavefront
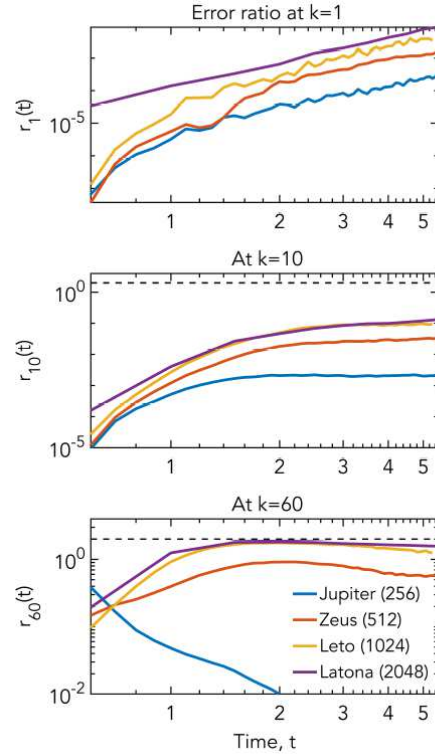
FIG. 10. Relative kinetic energy error as a function of time at a fixed wavenumber for Jupiter (256), Zeus (512), Leto (1024) and Latona (2048). From left to right, $k \in \{1, 10, 60\}$.
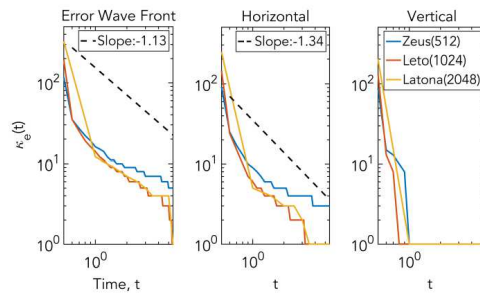

FIG. 11. Isotropic, horizontal and vertical error wave front for Zeus (512), Leto (1024) and Latona (2048). The reference line is a linear fit of Leto (1024).

posses a slope closer to the stationary isotropic turbulence studied by Métais and Lesieur (1986) than their decaying case, which could be a direct consequence of the anisotropy of our experiments. We can appreciate that both Leto (1024) and Latona (2048) present a faster upscale propagation compared with Zeus (512), which mirrors our previous discussion indicating that there may exist a phenomenological jump from Zeus (512) to Leto (1024).

C. Error introduction

Several questions may naturally arise regarding the aforementioned results and their applicability under diverse conditions. In particular, how exactly does the specific choice of noise addition influence the final outcome of the numerical experiments? In any predictability study, the implications of this issue are crucial, as they provide robustness and generality to the results. This section is concerned with dissecting that question and providing a reply to some of the natural inquiries related to error introduction. For instance, all the experiments in section III B have shared the same wavenumber error cutoff at $k_c = 20$, while changing the amplitude of the random perturbations accordingly so that all experiments share the same amount of initial error. In the stratified turbulence realm this could have great significance given the existence of a transitional scale such as the Ozmidov wavenumber. It may be the case that the error dynamics present some kind of conversion if the cutoff wavenumber is placed behind or ahead of that threshold.

1. Wavenumber cutoff dependency

Let's start exploring the sensitivity of the predictability results with respect to the wavenumber cutoff selection. Our approach is fairly simple, taking the base experiment, Leto (1024), and selecting a different cutoff wavenumber $k_c \in \{20, 40, 60, 80\}$[1], while still keeping the same amount of total initial error and the same parameters such as stratification, viscosity, etc.

This fact lead us to figure 12, which shows the error ratio spectra. The highlighted initial spectrum across the panels of figure 12 is the only spectrum that depends on k_c. Note that the initial spectrum changes in height as a mere consequence of the condition of having the same total initial error. Besides that initial spectrum, the strong resemblance of the spectra is uncanny. We have omitted the horizontal and vertical decomposition of the error and ratio spectra, as the nearly indistinguishable tendency continues within the spectral analysis of these quantities as well. Conversely, it is worth remembering that the Ozmidov wavenumber for these experiments takes a

---

[1] An important remark is that we kept the same unperturbed twin (Apollo) for all the following experiments, and we just run modified versions of Artemis.

value of $k_O = 50$ and there is no discernible change at either of the spectral diagnostics when we sweep the cutoff wavenumber through that value.
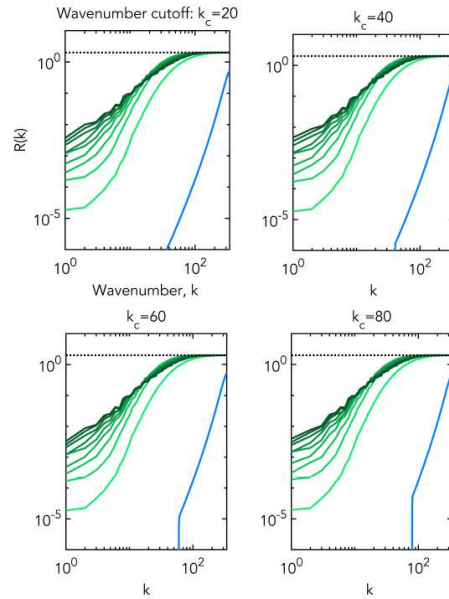

FIG. 12. Ratio energy spectra of the modified Leto (1024) experiment with cutoff wavenumbers at $k = 20, 40, 60, 80$. The initial ratio spectrum is highlighted in blue.

Moving on, in figure 13 we present the total error and error wavefront time series for simulations with different k_c. The total error of each experiments ends up being identical again, as is the case with the error wavefront. This result is quite remarkable, as it implies that both on the local and global scale, the experiments undeniably share the same error propagation characteristics. The overall conclusion is that there is no correlation or dependency between the studied range of cutoff wavenumbers and the final outcome of the experiments.

One is definitely tempted to push a little further the studied range, insomuch as to know what would be the consequences of inserting the perturbations at the region mostly characterized by the inverse cascade of error, setting $k_c \sim 10$ for example.

2. Geometrical implications: Cylinder v. Sphere

Another question is how our results depend on the geometry of the error introduction. Our numerical experiments add random noise with a pre-established amplitude for all wavenumbers beyond the cutoff wavenumber (*i.e.* for all **k** in our nu-
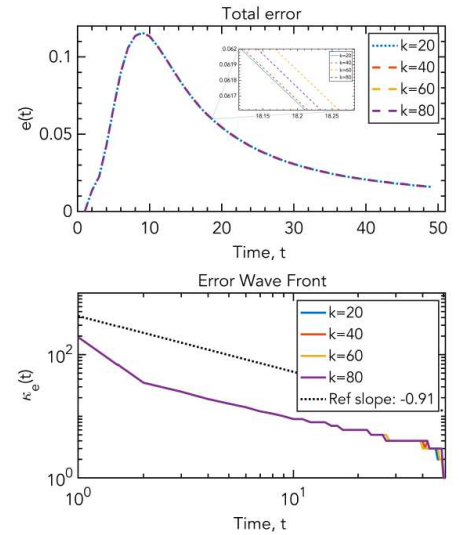

FIG. 13. Time series of the total error and error wavefront for the modified Leto (1024) experiment with cutoff wavenumbers at $k_c = 20, 40, 60, 80$.

merical domain such that $k_x^2 + k_y^2 + k_z^2 \geq k_c^2$). This means that we are uniformly adding random perturbations to the velocity field at each grid-point of our cubic Fourier domain outside the sphere of radius k_c, which is reasonable given the isotropic initial conditions but presents a clear asymmetry when dealing with anisotropic stratified turbulence. Now, it is natural to ponder whether this spherical geometry of error introduction can expressively alter the amount of error that is injected into each level of what would later become the layered structure. This inquiry leads us to present another modification to our base case, changing the geometry of the error introduction from the domain-complement of a sphere, to the domain-complement of a cylinder (*i.e.* for all **k** in our numerical domain such that $k_x^2 + k_y^2 \geq k_c^2$) while modifying the noise amplitude in order to keep the same total initial error as our reference experiment. In that way, all the horizontal planes in the wave vector domain are supplied with approximately the same amount of initial error.

Similarly to the case of the modified cutoff wavenumbers, we find no dependence on the error introduction geometry except for the initial error spectrum. The horizontal spectra of error energy effectively showed that there is a uniform amount of initial error insertion at each horizontal plane (not shown). Regardless, we obtain practically the same result in every subsequent spectrum. For the vertical error spectra, even the initial spectrum is indistinguishable. Moving on, the 3D error ratio spectra were calculated accordingly, but they are not displayed due to their inability to add something different to the
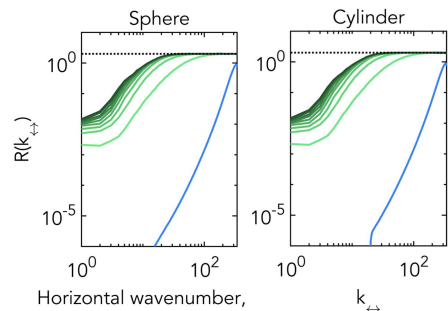
FIG. 14. Horizontal error ratio spectra of Leto (1024) with spherical and cylindrical complement error addition.
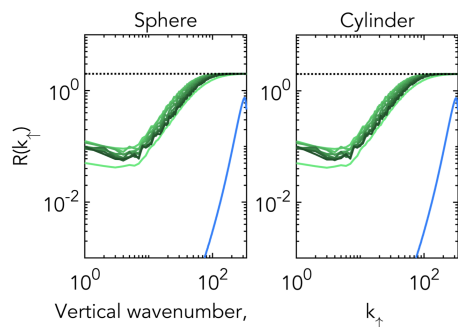

FIG. 15. Vertical error ratio spectra of Leto (1024) with spherical and cylindrical complement error addition.
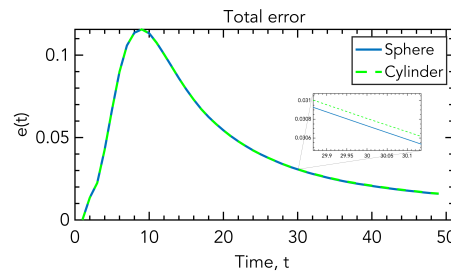

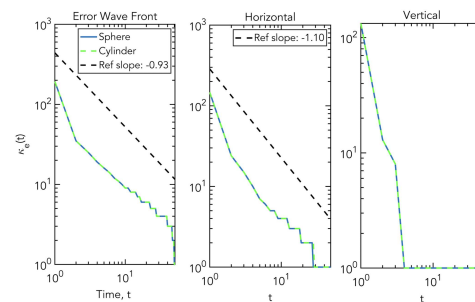FIG. 16. Total error time series of Leto (1024) with spherical and cylindrical complement error addition.

FIG. 17. Isotropic, horizontal and vertical error wave front for Leto (1024) with spherical and cylindrical complement error addition.

discussion. In figure 14 and figure 15, we present the horizontal and vertical error ratio spectra, respectively, for the spherical and cylindrical cases. Specifically, in the horizontal case, we can distinguish between the two cases in the initial spectrum: in the cylindrical case, we observe a step function as there is no error contribution at any $k_\leftrightarrow < 20$, while in the vertical case, there is still no discernible distinction between both geometries. We present figure 16 and figure 17 to complete the picture that both at the local and global scales, the experiments present the same error growth characteristics. There is no visible dependence on the geometry of the error introduction both on the total error time series nor in the error wavefront.

The overall results presented in this section strongly suggest that the total amount of error likely carries a more significant weight in the error dynamics compared to the geometrical implications of error introduction and wavenumber cutoff.

IV. SUMMARY AND DISCUSSION

Predictability studies have been built upon Lorenz's original scheme since its conception and have been developed to analyze predictability on a wide variety of fluid systems. Such a framework establishes that certain systems possess an intrinsic range of predictability not extendable by reducing the initial error of observation. In these cases, errors at the smallest scales lead to progressive error propagation toward larger scales, termed an inverse cascade of error, closely related to the system's kinetic energy spectrum slope. Stratified turbulence's anisotropy and different slopes for isotropic and horizontal kinetic energy spectra at various buoyancy Reynolds numbers present an opportunity to apply the classical analysis to this rich problem.

Near-identical twin simulations studied the effects of buoyancy Reynolds number on predictability of decaying stratified turbulence, displaying vortical layered structures and approaching $k_\leftrightarrow^{-5/3}$ energy spectra with increasing Re_b. Predictability diagnostics showed an inverse cascade of error on both isotropic and horizontal wavenumbers, with characteristic regions dominated by inverse cascade at large scales and decay at intermediate scales. A scale balancing both regions

remains stable with respect to Re_b.

We qualitatively corroborated self-similar error spectra evolution and the decorrelation being independent of the cutoff scale for error introduction, which aligns well with the results of the aforementioned classical school of predictability (e.g. Lilly, 1972; Leith and Kraichnan, 1972; Herring et al., 1973), noting uniform error propagation on vertical scales. Error ratio spectra revealed error saturation at various wavenumbers regardless of inverse cascade existence, expanding with higher Re_b. Error wavefront analysis showed negative power law progression, faster with higher Re_b, reducing predictability. These findings are in line with with the picture of stratified turbulence, developed e.g. by Brethouwer et al. (2007), as having a direct energy cascade from large to small horizontal scales. Experiments exhibited independence regarding error introduction and geometry, indicating total initial error's greater importance. The insensitivity of predictability to the scale of error introduction is consistent with the picture of Lorenz (1969).

Similar to the results presented by Chollet and Métais (1989), we infer that the upscale transfer of error is local, in terms of spectral space, and presumably dominated by interactions between similar scales, as shown by the wavefront error resemblance. Additionally, we have built upon the main objective of Morss et al. (2009), of exhibiting a link between the steepness of spectral slopes and the error growth dynamics. In line with the conclusions of Ngan et al. (2009), our results reinforce the point of predictability being a function of scale and subject to dimensionless parameters, such as Re_b, in our case, for stratified turbulence. Nevertheless, we were not able to effectively confirm the existence of an exponential initial growth of error for our experiments, as it was the presented in previous studies like Boffetta and Musacchio (2017) and Ge et al. (2023).

Our results underscore the limited predictability of small-scale atmospheric and oceanic turbulence, where stratification is strong but rotation is weak, and for large-eddy simulations where parameterized sub-grid scale turbulence can be understood as error with a grid-scale cutoff. This work can be further extended by investigating the dependence on Fr of experiments with similar buoyancy Reynolds number achieved through different parameter combinations. One approach would be to vary the stratification (represented by buoyancy frequency) while keeping viscosity constant in experiments with the same resolution. This would isolate the effect of stratification on Fr for a given Re_b. Future work may explore extending schemes to forced stratified turbulence to further analyze the effects of the buoyancy Reynolds number under stationary conditions, removing the decay phase and achieving error saturation at the largest scales. Considering more variants of error introduction such as anisotropic perturbations or addition of colored noise, like the Ornstein–Uhlenbeck process as perturbations to velocity fields, could provide more realistic implications. Furthermore, exploring how different initial conditions and boundary conditions influence predictability in stratified turbulence systems could enhance our understanding of the phenomenon.

DATA AVAILABILITY STATEMENT

The data that support the findings of this study are available from the corresponding author upon reasonable request.

P. Billant and J.-M. Chomaz. Experimental evidence for a new instability of a vertical columnar vortex pair in a strongly stratified fluid. *J. Fluid Mech.*, 418:167–188, 2000.

G. Boffetta and S. Musacchio. Predictability of the inverse energy cascade in 2 d turbulence. *Phys. Fluids*, 13(4):1060–1062, 2001.

G. Boffetta and S. Musacchio. Chaos and predictability of homogeneous-isotropic turbulence. *Phys. Rev. Lett.*, 119, 2017.

G. Brethouwer, P. Billant, E. Lindborg, and J.-M. Chomaz. Scaling analysis and simulation of strongly stratified turbulent flows. *J. Fluid Mech.*, 585: 343–368, 2007.

J.-P. Chollet and O. Métais. Predictability of three dimensional turbulence in large eddy simulation. *Eur. J. Mech. B/Fluids*, 8:523–548, 1989.

T. M. Dillon and D. R. Caldwell. The batchelor spectrum and dissipation in the upper ocean. *J. Geophys. Res. Oceans*, 85(C4):1910–1916, 1980.

D. R. Durran. *Numerical Methods For Fluid Dynamics With Applications To Geophysics.* Springer, 2nd edition, 2010.

D. R. Durran and M. Gingrich. Atmospheric predictability: Why butterflies are not of practical importance. *J. Atmos. Sc*, 71(7):2476 – 2488, 2014.

A. E. Gargett, T. R. Osborn, and P. W. Nasmyth. Local isotropy and the decay of turbulence in a stratified fluid. *J. Fluid Mech.*, 144:231–280, 1984. doi: 10.1017/S0022112084001592.

J. Ge, J. Rolland, and J. C. Vassilicos. The production of uncertainty in three-dimensional navier–stokes turbulence. *J. Fluid Mech.*, 977:A17, 2023. doi:10.1017/jfm.2023.967.

J. R. Herring, J. J. Riley, G. S. Patterson, and R. H. Kraichnan. Growth of uncertainty in decaying isotropic turbulence. *J. Atmos. Sci*, 30(6), 1973.

E. Kalnay. *Atmospheric Modeling, Data Assimilation and Predictability.* Cambridge University Press, 2002.

Y. Kimura and J. R. Herring. Diffusion in stably stratified turbulence. *J. Fluid Mech*, 328:253–269, 1996.

A. N. Kolmogorov. The local structure of turbulence in incompressible viscous fluid for very large Reynolds number. *Dok. Akad. Nauk. SSSR*, 30: 301–305, 1941.

R. H. Kraichnan. Inertial Ranges in Two-Dimensional Turbulence. *The Phys. Fluids*, 10(7):1417–1423, 07 1967. ISSN 0031-9171. doi: 10.1063/1.1762301.

J. D. Legaspi and M. L. Waite. Prandtl number dependence of stratified turbulence. *J. Fluid Mech*, 903:A12, 2020. doi:10.1017/jfm.2020.619.

C. E. Leith. Atmospheric predictability and two-dimensional turbulence. *J. Atmos. Sci*, 28:145–161, 1971.

C. E. Leith and R. H. Kraichnan. Predictability of turbulent flows. *J. Atmos. Sci*, 29(6):1041 – 1058, 1972.

D. K. Lilly. Numerical simulation studies of two-dimensional turbulence: Ii. stability and predictability studies. *Geophys. Fluid Dyn.*, 4(1):1–28, 1972.

J. T. Lin and Y. H. Pao. Wakes in stratified fluids: A review. *Annu. Rev. Fluid Mech.*, 11:317–338, 1979.

E. Lindborg. The energy cascade in a strongly stratified fluid. *J. Fluid Mech.*, 550:207–242, 2006.

C.-L. Liu, A. Kaminski, and W. Smyth. The butterfly effect and the transition to turbulence in a stratified shear layer. *J. Fluid Mech.*, 953:A43, 12 2022.

K. W. Lo and K. Ngan. Predictability of turbulent flow in street canyons. *Bound.-Layer Meteorol.*, 156(2):191–210, Aug 2015.

E. N. Lorenz. The predictability of a flow which possesses many scales of motion. *Tellus*, 21(3):289–307, 1969.

T. S. Lundgren. Kolmogorov turbulence by matched asymptotic expansions. *Phys. Fluids*, 15(4):1074–1081, 2003.

A. Maffioli and P. A. Davidson. Dynamics of stratified turbulence decaying from a high buoyancy Reynolds number. *J. Fluid Mech.*, 786:210–233, 2016.

R. E. Morss, C. Snyder, and R. Rotunno. Spectra, Spatial Scales, and Predictability in a Quasigeostrophic Model. *J. Atmos. Sci*, 66(10), 2009.

O. Métais and M. Lesieur. Statistical predictability of decaying turbulence. *J. Atmos. Sci*, 43(9):857 – 870, 1986.

K. Ngan, P. Bartello, and D. N. Straub. Predictability of rotating stratified turbulence. *J. Atmos. Sc*, 66(5), 2009.

W. L. Oberkampf, S. M. DeLand, B. M. Rutherford, K. V. Diegert, and K. F. Alvin. Error and uncertainty in modeling and simulation. *Reliab. Eng. Syst. Saf.*, 75:333–357, 2002.

L. F. Richardson. *Weather Prediction by Numerical Process*. Cambridge University Press, 1922.

J. J. Riley and S. M. deBruynKops. Dynamics of turbulence strongly influenced by buoyancy. *Phys. Fluids*, 15:2047–2059, 2003.

J. J. Riley and M.-P. Lelong. Fluid motions in the presence of strong stable stratification. *Annu. Rev. Fluid Mech.*, 32:613–657, 2000.

J. J. Riley and E. Lindborg. Stratified turbulence: A possible interpretation of some geophysical turbulence measurements. *J. Atmos. Sci.*, 65:2416–2424, 2008.

J. J. Riley and E. Lindborg. Recent progress in stratified turbulence. In *Ten Chapters in Turbulence*, pages 269–317. Cambridge University Press, 2012.

R. Rotunno and C. Snyder. A generalization of lorenz's model for the predictability of flows with many scales of motion. *J. Atmos. Sc*, 65(3):1063 – 1076, 2008.

Y.Q. Sun and F. Zhang. A new theoretical framework for understanding multiscale atmospheric predictability. *J. Atmos Sci.*, 77(7):2297 – 2309, 2020.

G. I. Taylor. Statistical theory of turbulence. *Proc. R. Soc. London, Ser. A*, 151:421–444, 1935.

P. D. Thompson. Uncertainty of initial state as a factor in the predictability of large scale atmospheric flow patterns. *Tellus*, 9(3):275–295, 1957.

J. J. Tribbia and D. P. Baumhefner. Scale interactions and atmospheric predictability: An updated perspective. *Monthly Weather Review*, 132(3), 2004.

M. L. Waite. Direct numerical simulations of laboratory-scale stratified turbulence. In T. von Larcher and P. D. Williams, editors, *Modelling Atmospheric and Oceanic Flows: Insights from Laboratory Experiments and Numerical Simulations*, pages 159–175. American Geophysical Union, 2014.

M. L. Waite. Dependence of model energy spectra on vertical resolution. *Mon. Wea. Rev.*, 144(4):1407–1421, 2016.

M. L. Waite and P. Bartello. Stratified turbulence dominated by vortical motion. *J. Fluid Mech.*, 517:281–308, 2004.

M. L. Waite and P. K. Smolarkiewicz. Instability and breakdown of a vertical vortex pair in a strongly stratified fluid. *J. Fluid Mech.*, 606:239–273, 2008. doi:10.1017/S0022112008001912.

K. Yoshimatsu and T. Ariki. Error growth in three-dimensional homogeneous turbulence. *JPSJ*, 88(12):124401, 2019.